Mott transition and antiferromagnetism of cold fermions in the decorated honeycomb lattice

Heng-Fu Lin,[*] Yao-Hua Chen, Hai-Di Liu, Hong-Shuai Tao, and Wu-Ming Liu

Beijing National Laboratory for Condensed Matter Physics, Institute of Physics, Chinese Academy of Sciences, Beijing 100190, China

We investigate two-component ultracold fermions loaded in a decorated honeycomb lattice described by the Hubbard model with repulsive interactions and nearest-neighbor hopping. The phase transitions are studied by combining the cellular dynamical mean-field theory with the continuous-time quantum Monte Carlo method. For weak interactions, the quadratic band crossing point is broken to a linear band crossing point and the system becomes a semimetal. With increasing interaction, the system undergoes a first-order phase transition to an antiferromagnetic Mott insulator at low temperatures. Below the critical temperature, due to the charge nematic fluctuation, a nematic metal forms between the semimetal and the antiferromagnetic Mott insulator. The effects of lattice anisotropy are also addressed. Furthermore, we discuss how to detect these phases in real experiments.

I. INTRODUCTION

Ultracold atoms in optical lattices are convenient and powerful systems for quantum simulations of condensed materials [1–3] in recent years. They have been used to study the BCS-BEC crossover, quantum magnetism, disorder, and nonequilibrium dynamics. For example, quantum magnetism has been simulated by a recent experiment with ultracold ^{40}K prepared in a mixture of two hyperfine states [4], and there are experimental signs of a Mott insulator [5,6]. To simulate those many-body phenomena is very challenging. Many models, which are important but not well studied in condensed-matter systems, are used to investigate ultracold atoms. The Hamiltonian of interacting ultracold atoms on a lattice can be given by the Hubbard model, which captures the physics of antiferromagnetism, Mott-insulator transition [7], and high-temperature superconductivity [8]. In order to search more exotic quantum phases in various systems, many different optical lattice geometries are created in cold-atom experiments, such as the triangle lattice, honeycomb lattice, and kagome lattice. In a given lattice with the unit cell consisting of multiple sites, the multiband or sublattices can cause fundamental problems in characterizing its preferred electronic many-body phases.

In recent years, many novel phases driven by the correlation effect have been found in two-dimensional (2D) multiband fermionic systems with a band crossing point, such as heavy-fermion behavior [9,10], superconductivity [11], and spin liquids [12–15]. The interesting phenomena existing in systems with a linear band crossing point at the Fermi surface have been widely studied, especially the Hubbard model in the honeycomb lattice. In these systems, the low-energy physics can be described by a Dirac fermion [16]. However, the physical property of a system with a quadratic band crossing point is still unclear, which can be observed in the decorated honeycomb lattice [17,18] and checker-board lattice [19,20]. Usually, quadratic band crossing points are protected by time-reversal symmetry, C_4 or C_6 rotational symmetry in the noninteracting limit. Previous mean-field theory [19] and functional renormalization-group approach [21] studies

show that many instabilities driven by the interaction can be observed in a system with quadratic band crossing points. These instabilities lead to many symmetry-broken phases, such as the quantum anomalous Hall phase, the quantum spin Hall phase, the nematic phase, and the spin nematic phase.

The decorated honeycomb lattice, which is also known as the star lattice, is a "cousin" of both the honeycomb lattice and the kagome lattice. It can be viewed as an "interpolating" lattice between the honeycomb lattice and the kagome lattice: if one shrinks the triangles at the vertices of the underlying honeycomb lattice to their center points, a honeycomb lattice is recovered, while expanding the triangles until their corners touch produces a kagome lattice. This structure has been found in a new polymeric iron(III) acetate [22]. The progress in experiments and theories on the optical lattice might provide a promising way to simulate a model. We can trap ultracold atoms in a decorated honeycomb lattice, the interaction between the trapped atoms is adjusted by the Feshbach resonance, and the hopping energy can be tuned by the lattice depth. Various novel phases are expected to be found in these systems, such as a chiral spin liquid [17] with time-reversal symmetry spontaneously broken in the Kitaev model, nonmagnetic order [23] in a spin-1/2 Heisenberg antiferromagnet, topological phases [18], and interaction-driven topological insulators [24]. Previous studies have mostly been dedicated to the spin fluctuation of effective spin models on a decorated honeycomb lattice, which can be found in many synthesized nanomaterials, such as the triangular organic material κ-BEDT(CN)$_3$ [13], kagome lattice herbertsmithite [25], and three-dimensional hyperkagome lattice magnet (Na$_4$Ir$_3$O$_8$) [26]. However, a quadratic band crossing point in a noninteracting system has many instabilities for interactions, leading to many novel phases. It is desirable to investigate the phase transitions of interacting fermions in this lattice, including both charge fluctuation and spin fluctuation.

In this work, we investigate the correlation effects of two-component fermionic atoms on a decorated honeycomb lattice by employing the cellular dynamical mean-field theory [27] combined with the continuous-time quantum Monte Carlo method [28]. We have obtained phase diagrams of the effect of the interaction U, lattice anisotropy λ, and temperature T. The antiferromagnetic insulator (AFI) phase, which is

---

*hflin@iphy.ac.cn

indicated by an antiferromagnetic order and a finite charge gap, is found when the interaction U is larger than the critical value U_{c2}. A semimetal (SM) is found when the interaction U is smaller than the critical interaction U_{c1}, in which the rotational symmetry is broken. And the nematic metal (NM) phase, which is induced by the charge nematic fluctuation [29,30] forming between the AFI and the SM, is identified by the anisotropic momentum-resolved spectrum. The NM-phase region can be enlarged by the lattice anisotropy. At high temperatures, all these phases are destroyed by thermal fluctuation. These interesting phases can be probed by time-of-fight images [31], noise correlation [32,33] from time-of-flight images, Raman spectroscopy [34], Bragg spectroscopy [35], and other experiments.

Our paper is organized as follows. In Sec. II, the model Hamiltonian is introduced, and its noninteracting properties and the cellular dynamical mean-field theory method are discussed. In Sec. III, we present the main results, including the Mott phase transition and magnetic properties driven by the interaction and isotropic hopping. In Sec. IV, the effect of the anisotropic hopping on the phase transition is discussed. In Sec. V, we discuss the experimental signatures on the detection of these novel phases in future cold-atom experiments, while Sec. VI is dedicated to concluding remarks.

II. THE MODEL AND CELLULAR DYNAMICAL MEAN-FIELD THEORY

We consider two-component fermions trapped in the decorated honeycomb optical lattice with nearest-neighbor hopping t on vertex triangles and t' ($t' = \lambda t$) between triangles shown in Fig. 1(a). Throughout the paper $t = 1$ defines the energy scale. The Hubbard model Hamiltonian can be written as

$$H = -t \sum_{\langle ij \rangle \sigma \triangle} c_{i\sigma}^{\dagger} c_{j\sigma} - t' \sum_{\langle ij \rangle \sigma \triangle \to \triangle} c_{i\sigma}^{\dagger} c_{j\sigma}$$
$$- \mu \sum_{i\sigma} n_{i\sigma} + U \sum_i n_{i\uparrow} n_{i\downarrow}, \qquad (1)$$

where $c_{i\sigma}^+$ and $c_{i\sigma}$ are the creation and the annihilation operators of electrons with spin index σ at site i, $n_{i\sigma} = c_{i\sigma}^+ c_{i\sigma}$ is the density operator, and $\triangle$ represents the vertex triangle. U is the on-site repulsion interaction, which can be adjusted by the Feshach resonance, and μ is the chemical potential. The Hamiltonian respects SU(2) spin symmetry, time-reversal symmetry, and C_6 lattice rotational symmetry. There are six sites in each unit cell, with two sublattices, A and B, in the decorated honeycomb lattice [Fig. 1(a)]. The superlattice vectors in real space [(green) arrows in Fig. 1(a)] and vectors in reciprocal space [(red) arrows in Fig. 1(b)] are shown. The reduced first Brillouin zone is shown in Fig. 1(b), which is identical to the honeycomb lattice and kagome lattice.

Firstly, we consider the noninteracting case $U = 0$. By using an orthogonal transformation, the kinetic term of the Hamiltonian is diagonalized at each k, and we get a noninteracting energy dispersion with six bands. The bands are $\varepsilon_{1,2,4,5}(k) = -\frac{t}{2} \pm (\frac{9}{4}t^2 + t'^2 \pm tt' \sqrt{3 + 2\cos k_1 + 2\cos k_2 + 2\cos(k_1 - k_2)})^{1/2}$ and $\varepsilon_{3,6}(k) = t \pm t'$, where $k_1 = (2 + \sqrt{3})k_x$ and $k_2 = (1 + \frac{1}{2}\sqrt{3})k_x + (\frac{3}{2} + \sqrt{3})k_y$. For the $t' < \frac{3}{2}t$ case, bands $\varepsilon_3(k)$ and $\varepsilon_6(k)$ are flat over
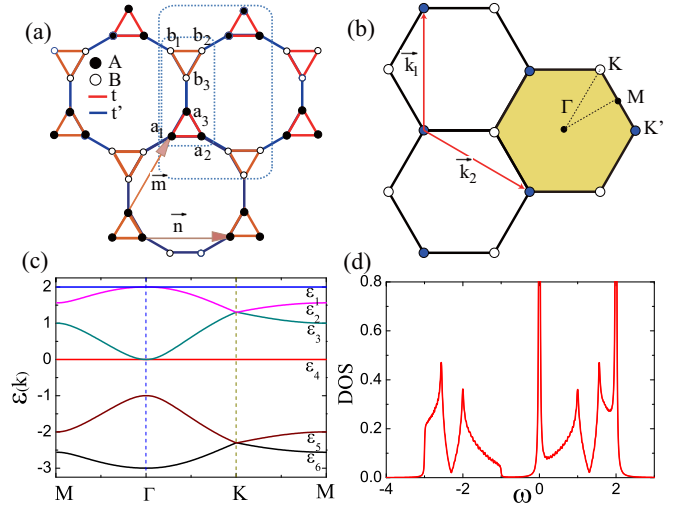

FIG. 1. (Color online) (a) Structure of the decorated honeycomb lattice. Filled circles denote the A sites; open circles, B sites. The unit cell contains six sites: a_1, a_2, a_3, b_1, b_2, and b_3. Inside the small rectangular area [dotted (blue) line] and large rectangular area [dotted (blue) line] are the 6- and 12-site clusters, respectively, used in our analysis. Arrows $\vec{m}$ and $\vec{n}$ are the real lattice vectors. (b) Reciprocal space vectors $\vec{k}_1$ and $\vec{k}_2$ and first Brillouin zone [shaded (yellow) hexagon] of the decorated honeycomb lattice. (c) Band structure of the tight-binding model along the path M-Γ-K-M shown in (b). There are six bands: ϵ_1, ϵ_2, ϵ_3, ϵ_4, ϵ_5, and ϵ_6. And there are Dirac points at K and K' (not shown) and the quadratic band crossing point at Γ. (d) Noninteracting density of states (DOS) of the system at half-filling $f = 1/2$. There are four van Hove singularities and two δ peaks.

the whole Brillouin zone. The dispersive bands $\varepsilon_1(k)$ and $\varepsilon_2(k)$ [$\varepsilon_4(k)$ and $\varepsilon_5(k)$] touch each other at K and K' with a linear dispersion, leading to Dirac points. However, bands $\varepsilon_3(k)$ and $\varepsilon_4(k)$ [$\varepsilon_6(k)$ and $\varepsilon_5(k)$] touch each other at Γ with a quadratic dispersion, leading to a quadratic band crossing point. For $t' > \frac{3}{2}t$, things are a little different. The flat band $\varepsilon_4(k)$ and the dispersive band $\varepsilon_5(k)$ touch each other at Γ with a quadratic dispersion, leading to a quadratic band crossing point. The six bands are shown in Fig. 1(c) along the various high symmetry directions. There are Dirac points at K and K' and a quadratic band crossing point at the Γ point. We can also define the noninteracting density of states (DOS) $\rho^0(\omega)$, including the chemical potential, as $\rho^0(\omega) = (1/N)\Sigma_{k,\alpha} 1/(\omega + \mu - \varepsilon_\alpha(k))$, where $\varepsilon_\alpha(k)$ is the band dispersion in this lattice. Figure 1(d) shows the $\rho^0(\omega)$ at half-filling and $t'/t = 1$. There is a δ-function peak at the Fermi surface and four van Hove singularities.

In this paper, we study the quadratic band crossing point's quantities in the Hubbard model for a decorated honeycomb lattice with filling factor $1/2$ and hopping amplitude $t' < \frac{3}{2}t$ first. In order to include nonlocal spatial fluctuations, we use the cellular dynamical mean-field theory (see the Appendix), which is the cluster extension of the dynamical mean-field theory. In our analysis, the 6- and 12-site clusters in Fig. 1(a) are used to set up the cluster Hamiltonian. Within cellular dynamical mean-field theory, the interacting lattice Green's function in the N_c-site basis is defined as $G(i\omega_n) = \sum_k [i\omega_n + \mu + t(k) - \Sigma(i\omega_n)]^{-1}$, where N_c is the

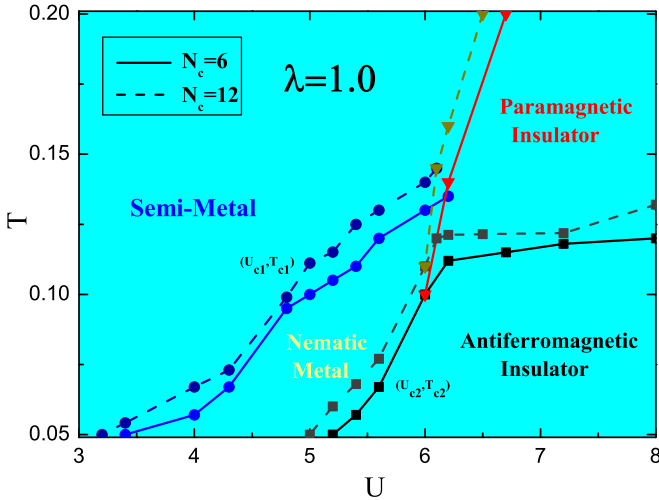FIG. 2. (Color online) Phase diagram for isotropic hopping ($\lambda = 1.0$) Hubbard model on a decorated honeycomb lattice as a function of U and T. Solid and dashed lines are the results obtained using the 6-site cluster ($N_c = 6$) and 12-site cluster ($N_c = 12$), respectively. There are four phases in the phase diagram: (i) semimetal (SM); (ii) antiferromagnetic insulator (AFI); (iii) nematic metal (NM); and (iv) paramagnetic insulator. The critical interaction and critical temperature of the SM-NM crossover are shown as (U_{c1}, T_{c1}). Critical points of the phase transition to AFI are shown as (U_{c2}, T_{c2}).

cluster size, $\omega_n = (2n + 1)\pi T$ are Matsubara frequencies, and $t(k)$ is the Fourier-transformed hopping matrix for the superlattice. $\Sigma(i\omega_n)$ represents the self-energy matrix in the site representation. The dynamical mean-field theory has contributed substantial theoretical progress in understanding the Mott transition, but not treating spatial fluctuation. Within the cellular dynamical mean-field theory, we can treat the frustration and nonlocal fluctuation more efficiently. Many works have been done to study the Mott transition and magnetic properties of various models, such as the full frustrated Hubbard model with different lattice structures, the model with relaxation of the frustration [36], and the frustrated kagome Hubbard model with heavy-fermion behavior [10].

III. FINITE-TEMPERATURE PHASE DIAGRAM WITH ISOTROPIC HOPPING

The finite-temperature phase diagram of the half-filling isotropic ($t' = t$) Hubbard model on a decorated honeycomb lattice obtained from the analysis using the six-site cluster is shown in Fig. 2. The results obtained using the 12-site cluster are also shown to quantitatively show the cluster-size dependence. At low temperatures, such as $T < T_{c1} \sim 0.1$, three phases are formed at different interaction strengths U. When $U < U_{c1} \sim 3.4$ at $T = 0.05$, the system is an SM. In this phase, the system has two Dirac points which are broken from the quadratic band crossing point, and the low-energy physics is described by the Dirac fermion. When $U > U_{c2} \sim 5.2$ and $T = 0.05$, the system undergoes a first-order phase transition to a Mott insulator phase with antiferromagnetic order. This is called the AFI phase. A nematic metal (NM) [37] emerges at intermediate interaction $U_{c1} < U < U_{c2}$, where U_{c1} and U_{c2} are the critical points of the SM-NM crossover and NM-
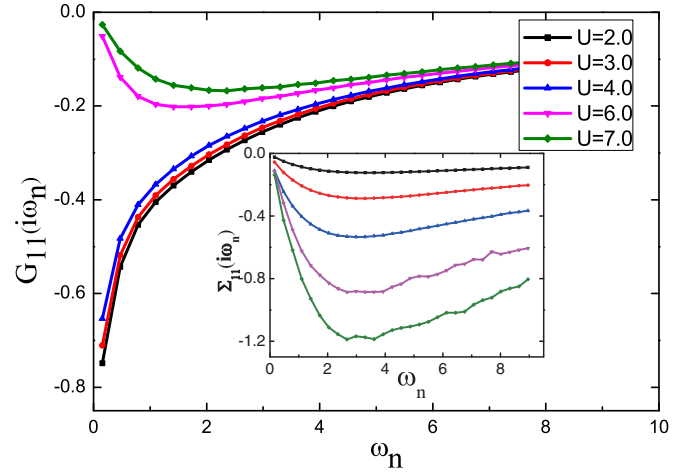

FIG. 3. (Color online) Enhancement of on-site self-energies across the semimetal and nematic metal transition with increasing U. The imaginary parts of the on-site propagator $G_{11}(i\omega_n)$ and on-site self-energy $\Sigma_{11}(i\omega_n)$ (inset) are plotted for different values of U when $T = 0.05$.

AFI phase transition, respectively. In this region, the system is metallic, which has an anisotropic momentum-resolved single-particle spectrum at the Fermi level and shows conventional Fermi-liquid behavior. With increasing temperature, the nematic order on the metal side and antiferromagnetic order on the insulator side can be gradually destroyed by the thermal fluctuation. The critical points (U_{c1}, T_{c1}) and (U_{c2}, T_{c2}), which indicate the breaking of the nematic order [(green) line with circles] and antiferromagnetic order phases (black lines with squares), are calculated. At very high temperatures, such as $T > T_{c1} = 0.13$, the nematic order and antiferromagnetic order have both been broken by the thermal fluctuation, and the system goes from SM crossover to paramagnetic insulator with increasing interaction. For example, at $T = 0.15$, the system are SM when $U < 6.2$ and paramagnetic insulator when $U > 6.2$. In the large, 12-site-cluster case, the properties of this system do not change, but the phase boundary shifts a little; for example, in $T = 1/20$, the phase transition of SM to NM is at $U = 3.2$ ($U = 3.4$ for the 6-site cluster), and the NM to antiferromagnetic Mott insulator transition is at $U = 5.0$ ($U = 5.2$ for the 6-site cluster).

To find more details about the correlation effects in this model, we calculate the on-site self-energy $\text{Im}\Sigma_{11}(i\omega_n)$ and propagator $\text{Im}G_{11}(i\omega_n)$. The imaginary part of the on-site self-energy $\text{Im}\Sigma_{11}(i\omega_n)$ and propagator $\text{Im}G_{11}(i\omega_n)$ provides information about the possible Fermi-liquid or non-Fermi-liquid behavior of the system as well as the nature of the charge gap opening [38,39]. In Fig. 3, we present $\text{Im}\Sigma_{11}(i\omega_n)$ and $\text{Im}G_{11}(i\omega_n)$ as a function of the Matsubara frequencies for different values of U at $T = 0.05$ and $\lambda = 1.0$ for a six-site cluster. When $U < U_{c2} \sim 5.2$, with decreasing ω_n, $\text{Im}\Sigma_{11}(\omega_n)$ increases while $\text{Im}G_{11}(\omega_n)$ decreases, $\text{Im}\Sigma_{11}(\omega_n \to 0) \to 0$ and $\text{Im}G_{11}(\omega_n \to 0) \to \text{const}$, which is similar to the Dirac fermion with a decreasing quasiparticle residue Z. For $U > U_{c2} \sim 5.2$ the behavior is clearly different; with decreasing ω_n, both $\text{Im}\Sigma_{11}(\omega_n)$ and $\text{Im}G_{11}(\omega_n)$ increase, $\text{Im}\Sigma_{11}(\omega_n \to 0) \to 0$ and $\text{Im}G_{11}(\omega_n \to 0) \to 0$, which implies that a gap
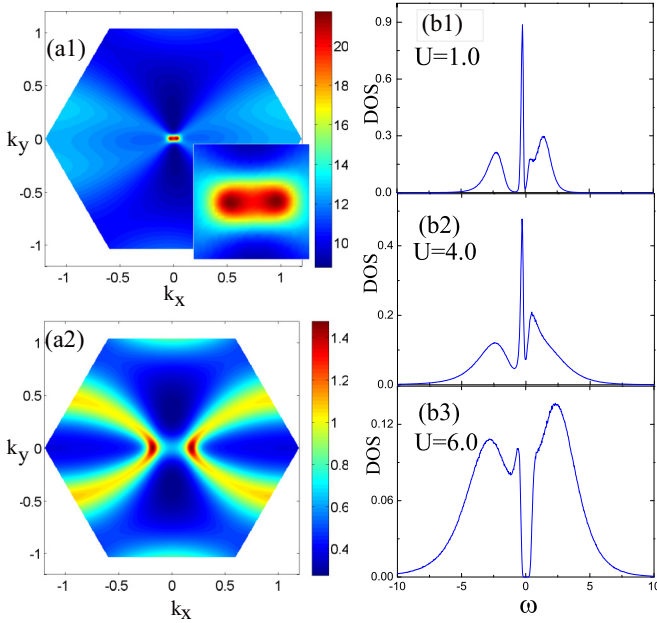
FIG. 4. (Color online) (a1, a2) Momentum-resolved spectral weight $A(k,0)$ at the Fermi level in the first Brillouin zone when $T = 0.05$. (a1) Semimetal phase when $U = 1.0$. Inset: Zoom-in of the spectral weight $A(k,0)$ around the center of the Brillouin zone. (a2) Nematic metal phase when $U = 4.0$. (b1–b3) DOS $\rho(\omega)$ at various interactions when $T = 0.05$. (b1) The zero density in the Fermi level at $U = 1.0$ shows that the system is a semimetal. (b2) A finite density in the Fermi level at $U = 4.0$, which indicates that the system stays in the nematic metal phase. (b3) A charge gap is opened at $U = 6.0$, which means that the system is an insulator.

exists near the Fermi level. The local component $\text{Im}\Sigma_{11}(i\omega_n)$ is enhanced with increasing interaction U. It has also been observed that the local components $\text{Im}\Sigma_{11}(i\omega_n)$ have no singularities and are proportional to ω_n in the low-energy region. The imaginary part of the self-energy $\text{Im}\Sigma_{11}(i\omega_n)$ approaches 0 as ω_n goes to 0 over the entire range of U. The quasiparticle picture can be used to describe the electronic states up to relatively large values of U. There are no non-Fermi-liquid properties in this system. The U dependence of the quasiparticle DOS at the Fermi level can also be defined as $\rho(0) = 1/\pi \text{Im} G_{11}(0)$. For $U = 2, 3, 4$, there is a finite DOS at the Fermi level, and the system is metallic. However, for $U = 6, 7$, the DOS approaches 0 at the Fermi level, and the system undergoes a phase transition to Mott insulator.

To see the single-particle excitation in the metallic region, we calculate the single-particle spectrum on the Fermi surface [40]. The momentum-resolved spectral weight at the Fermi level $A(k, \omega = 0)$ in the first Brillouin zone is investigated for different values of interaction U and temperature T. $A(k, \omega = 0)$ is obtained by $A(k, \omega = 0) \approx -\frac{1}{6\pi} \sum_{i=1}^{6} \lim_{\omega_n \to 0} \text{Im} G_{ii}(k, i\omega_n)$, where i is the site index within the chosen cluster. When $U = 0$, the Fermi surface $A(k,0)$ is a point at Γ, where the flat band $\varepsilon_3(k)$ and the dispersive bands $\varepsilon_4(k)$ touch each other with quadratic dispersions. When the interaction U is weak, such as $U < U_{c1} \sim 3.4$, the Fermi surface $A(k,0)$ breaks into two points, which implies that the system is an SM. Figure 4(a1) shows the Fermi surface

$A(k,0)$ at $U = 1.0$, $T = 0.05$. The unstable quadratic band crossing point in two dimensions split into two Dirac points very close to point Γ along any of the K-K' Brillouin-zone diagonals. This means that the system breaks the C_6 rotational symmetries to C_2 spontaneously, which was also found in Refs. [41] and [42]. When the interaction $U > U_{c1}$, the Fermi surface $A(k,0)$ is distributed in the first Brillouin zone. It is not along one of the K and K' Brillouin-zone diagonals. The Fermi surface $A(k,0)$ becomes anisotropic [see Fig. 4(b2)] at $U = 4.0$, $T = 0.05$. The anisotropic Fermi surface, which has been studied by means of cellular dynamical mean-field theory [36,43], indicates that the system becomes an NM.

In the nematic state the orientational symmetry of the system is spontaneously broken, without breaking of the translation invariance. A nematic phase can be obtained from a Pomeranchuk [44] instability generated by forward-scattering interactions in a normal metal. In the 2D Hubbard model with a next-nearest-neighbor hopping amplitude on a square lattice, the Fermi surface nesting is broken [45]. Moreover, a d-wave pairing instability driven by the antiferromagnetic spin fluctuations can be found. The pairing instability dominates over magnetic instabilities in the weak-coupling limit for any density, and strong forward-scattering interactions develop which may lead to a Pomeranchuk instability, breaking the tetragonal symmetry of the Fermi surface. The NM phase is also formed due to the instabilities of the quantic band crossing point caused by the interaction, leading to spontaneous breaking of the rotational symmetry. A system with a quantic band crossing point somewhere in its 2D Brillouin zone has already been discussed. In the lattice models of noninteracting fermions, the quantic band crossing points are protected by time-reversal symmetry and C_6 or C_4 rotational symmetry. The perturbative stability of a quantic band crossing point was studied for 2D noninteracting systems with C_4 symmetry [20]. For interacting fermions, it was noted that a quantic band crossing point in two dimensions has instabilities for arbitrarily weak interactions, leading to spontaneous breaking of the rotational symmetry (nematic phase) or time-reversal invariance [19,21]. The decorated honeycomb lattice is a system with a quantic band crossing point. A nematic state can be obtained from a Pomeranchuk instability generated by forward-scattering interactions in a normal metal, in which spacial rotational invariance C_6 is broken spontaneously.

In order to investigate the evolution of the single-particle spectrum in the phase transition more clearly, we calculate the local DOS for different U's when $T = 0.05$. The DOS is defined as $\rho(\omega) = -\frac{1}{6\pi} \sum_{i=1}^{6} \text{Im} G_{ii}(\omega + i\delta)$, where i is the site index within the cluster. The DOS can be derived from the imaginary-time Green's function $G(\tau)$ using the maximum entropy method [46]. When $U = 1.0$, in the SM region, the DOS is 0 at the Fermi level [see Fig. 4(b1)]. A similar phenomenon is found in the noninteracting DOS shown in Fig. 1(d); there are two regions in which the DOS is 0 at the linear band crossing point. When $U = 4.0$, corresponding to the NM, the DOS is finite and a pseudogap forms near the Fermi level [see Fig. 4(b2)]. The three spectral weight peaks gradually shift to a higher energy when the interaction increases. When $U = 6.0$, in the Mott insulator region, one of the spectral weight peaks is suppressed by interaction and a gap is opened near the Fermi energy [Fig. 4(b3)].
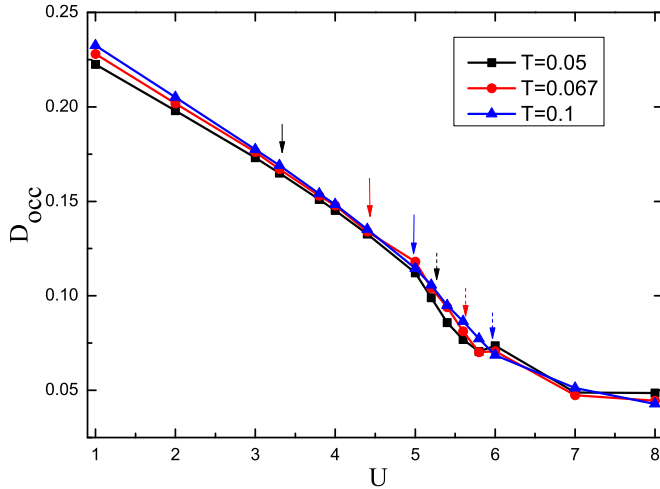
FIG. 5. (Color online) Evolution of double occupancy D_{occ} as a function of U for various T. Solid arrows show the critical points of SM-NM crossover. And the critical points of the NM-AFI phase transtion are shown by dashed arrows.

FIG. 6. (Color online) Evolution of the antiferromagnetic order parameter m and the single-particle gap ΔE as a function of U when $\lambda = 1.0$ and $T = 0.05$. Insets: (a) Evolution of m and ΔE as a function of U at $\lambda = 1.0$ and $T = 0.2$; (b, c) two equivalent antiferromagnetic spin configurations of the antiferromagnetic insulator in a decorated honeycomb lattice.

The double occupancy $D_{occ} = \partial F / \partial U$ for a six-site cluster are shown in Fig. 5, where F denotes the free energy. The double occupancy can be used to find the phase transition order due to the direct correlation with the free energy. The D_{occ} as a function of U is obtained by $D_{occ} = \frac{1}{N_c} \sum_{i=1}^{N_c} \langle n_{i\uparrow} n_{i\downarrow} \rangle$, where N_c is the site number of the cluster. We find that D_{occ} decreases smoothly at the critical point U_{SM-NM}. In both phases, the C_6 rotational symmetry is broken as discussed above. It is a crossover from the SM to the NM phase. However, a discontinuity can be observed near the critical point U_{NM-AFI}, which signals a first-order phase transition. In cold-atom experiments, first, the double occupancy can be used to characterize the metal insulator transition [4]; there is a significant increase in the double occupancy with atom number in the noninteracting regime, whereas upon entering the Mott insulating regime the double occupancy is suppressed. Second, double occupancy is a universal measure of antiferromagnetic correlations [47]. At low temperatures, a fermionic gas trapped in an optical lattice, which is half-filled, can form an antiferromagnetic core at the center. Meanwhile, the double occupancy can also be enhanced.

In order to investigate the evolution of magnetic order on a decorated honeycomb lattice, we define the antiferromagnetic order parameter $m = \frac{1}{N_c} \sum_i \text{sign}(i)(n_{i\uparrow} - n_{i\downarrow})$, where i is the site index [see Fig. 1(a)], and N_c is the site number of the cluster. $\text{sign}(i)$ is defined as $\text{sign}(i) = 1$ for sites a_1, $a_3(b_3)$, and b_2 and $\text{sign}(i) = -1$ for sites b_1, $b_3(a_3)$, and a_2. We also define the ferromagnetic order parameter, $\bar{m} = \frac{1}{N_c} \sum_i \text{sign}(i)(n_{i\uparrow} - n_{i\downarrow})$, where $\text{sign}(i)$ is defined as $\text{sign}(i) = 1$ for sites a_1, a_2, and a_3 and sites b_1, b_2, and b_3. It is found that the ferromagnetic order parameter is 0 all the time. Figure 6 shows the evolution of the antiferromagnetic order parameter m and charge gap ΔE as a function of the interaction strength U, at $\lambda = 1.0$ and temperature $T = 0.05$ for a six-site cluster. We find an AFI phase when $U > 5.2$, in which the magnetic order appears simultaneously with the charge gap. This means that the magnetic order enhances the
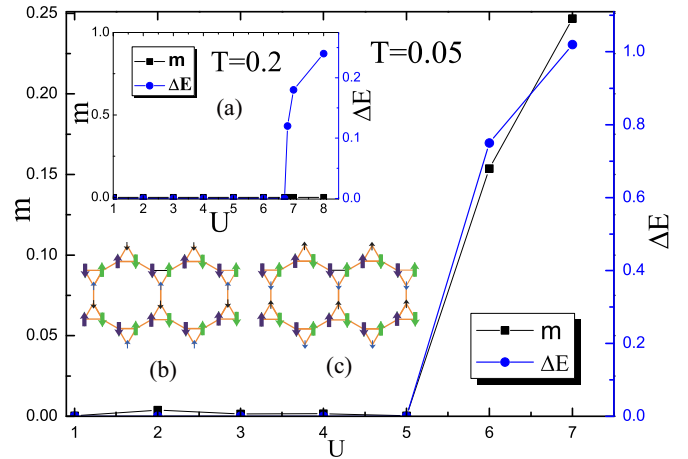
localization of electrons on the lattice sites. Two equivalent spin configurations of the AFI can be seen in insets (b) and (c) in Fig. 6. This finding is different from previous studies on a system with a flat band and a quadratic band crossing point, which favor a Nagaoka ferromagnetic phase [48] and nematic ferromagnetic. Inset (a) in Fig. 6 shows that there is no magnetic order when $T = 0.2$.

IV. THE PHASE DIAGRAM WITH ANISOTROPIC HOPPING

We now investigate the influence of the lattice anisotropy $\lambda = t'/t$ on the phase transitions in the decorated honeycomb lattice. For $\lambda < 1$, the effective hopping amplitudes on vertex triangles is larger than between vertex triangles, the electrons are more itinerant in the intra-triangles; for $\lambda > 1$, the effective hopping amplitudes on vertex triangles is smaller than between vertex triangles, the electrons are more itinerant in the inter-triangles. To determine the phase transition points while varying the interaction U for the fixed values of lattice anisotropy λ, we carefully calculate the momentum-resolved spectral, on-site self-energy and on-site green function at the low temperature. When $\lambda \neq 1$, the NM phase is enhanced.

Figure 7 shows the phase diagram in the lattice anisotropy λ and interaction U plane when temperature $T = 0.067$, which is obtained from the analysis using the 6-site cluster and the 12-site cluster. The phase boundary is shifted by the anisotropy λ. We find that $U_{c1} = 4.6$, $U_{c2} = 6.6$ when $\lambda = 1.2$ and $U_{c1} = 3.8$, $U_{c2} = 5.4$ when $\lambda = 0.8$ for the 6-site-cluster case. For the 12-site-cluster case, $U_{c1} = 4.6$, $U_{c2} = 6.6$ when $\lambda = 1.2$ and $U_{c1} = 3.8$, $U_{c2} = 5.4$ when $\lambda = 0.8$. The region of the NM phase is enlarged when λ varies. This means that the NM becomes more stable due to the enhanced anisotropy. This provides a way to realize such a state in materials and to detect this phase in cold-atom experiments.
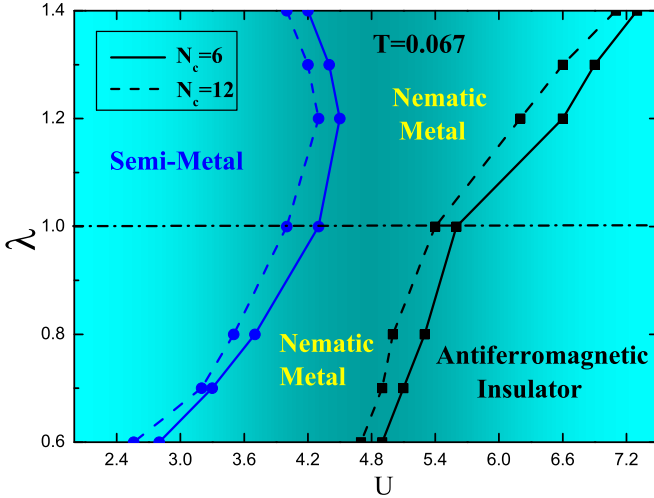
FIG. 7. (Color online) Phase diagram of the Hubbard model on a decorated honeycomb lattice as a function of U and the lattice anisotropy λ when $T = 0.067$. Solid and dashed lines are the results obtained using the 6-site cluster ($N_c = 6$) and 12-site cluster ($N_c = 12$), respectively. Leftmost (blue) lines show the phase crossover line of the semimetal and nematic metal; circles indicate critical points. Rightmost (black) lines show the phase translation line of the nematic metal and antiferromagnetic insulator; squares indicate critical points.

V. EXPERIMENTAL SIGNATURES

Besides being of fundamental theoretical interest, these phases are of broad experimental relevance. The NM, which is similar to the electronic nematicity observed in iron pnictide [49,50] and copper oxide [51,52] high-temperature superconductors, can be found in other strongly correlated materials and can be probed by angle-resolved photoemission spectroscopy (ARPES) [53], neutron scattering, and nuclear magnetic resonance [54]. The AFI phase have been found in the polymeric iron(III) acetate [22] of the same lattice structure can be detected using neutron scattering and nuclear magnetic resonance [54].

In ultracold-atom systems, both the interaction and the hopping amplitude can be fully controlled by using Feshbach resonance and changing the lattice depth, respectively. Therefore, this model can be realized and these phases can also be detected using cold-atom detecting technology, such as time-of-flight images [31], Raman spectroscopy [34], and Bragg spectroscopy [35]. Using absorption imaging technology, physical quantities such as the double occupancy and Fermi surface can be obtained for analysis of the system. And the double occupancy can be measured using the following experimental procedure: (1) Rapidly increaseg the depth of the optical lattice to $30E_r$ to inhibit further tunneling. (2) Shift the energy of atoms at doubly occupied sites by approaching a Feshbach resonance. Then use a radiofrequency pulse to transfer one of the spin components to a third, only at doubly occupied sites. (3) Use the absorption images to obtain the fraction of transferred atoms, and deduce the double occupancy.

Because of the intrinsic inhomogeneity of atomic clouds, observables routinely measured in solids, e.g., x-ray or neutron diffraction, may be hard to access in cold-atom-based system. The detection of the antiferromagnetic order parameter

via noise correlation [32,33] or Bragg spectroscopy [35] is nontrivial. It is essential to identify fingerprints of the antiferromagnetic phase that are easily accessible in current experiments, such as the double occupancy or Fermi surface. The current experimental limit to the entropy per particle for a two-component system is $S \approx 0.77 k_B$. The corresponding temperature scale is $T \approx t$, which is still higher than the antiferromagnetic superexchange energy J [5]. For detecting antiferromagnetism, we can facilitate Pomeranchuk cooling to temperatures comparable to the superexchange energy scale.

VI. SUMMARY

In summary, we have derived the phase diagram of correlated two-component fermions on a decorated honeycomb lattice as a function of the temperature T, interaction U, and anisotropy λ. For a weak interaction $U < U_{c1}$ (such as $U_{c1} = 3.6$ for the six-site cluster when $T = 0.05$), the system breaks into an SM phase. An NM phase with an anisotropic momentum-resolved single-particle spectrum at the Fermi level is found when $U_{c1} < U < U_{c2}$ (such as $U_{c1} = 3.6$, $U_{c2} = 5.2$ for the six-site cluster when $T = 0.05$), above the SM phase. The NM breaks the C_6 symmetry and the phase region is enlarged when the lattice anisotropy increases. When $U > U_{c2}$ (such as $U_{c2} = 5.2$ for the six-site cluster when $T = 0.05$), the system undergoes a first-order phase transition from the gapless NM to a gapped AFI. The NM and AFI phases disappear due to the strong thermodynamic fluctuation at high temperatures (such as $T > 0.13$ at $\lambda = 1.0$ for the six-site cluster). Our studies provide a helpful step toward understanding the charge fluctuation and magnetic fluctuation in the metal-insulator transition, which are of relevance to the magnetic order phase and charge order phase in multiband systems with a quadratic band crossing point.

APPENDIX: METHODS

The cellular dynamical mean-field theory is an extension of the dynamical mean-field theory, which is able to partially cure the dynamical mean-field theory's spatial limitations. We replace the single-site impurity with an N_c-site cluster of impurities embedded in a self-consistent bath. Short-ranged spatial correlations are in this way treated exactly inside the cluster, and the first momentum dependence of the properties of the system is recovered. The cluster-impurity problem embedded in a bath of free fermions can be written in a quadratic form,

$$S_{\text{eff}} = \int_0^\infty \sum_{ij\sigma} c_{i\sigma}^\dagger \mathcal{G}_{ij\sigma}^{-1}(\tau) c_{j\sigma} + U \int_0^\beta dt \sum_i n_{i\uparrow}(\tau) n_{i\downarrow}(\tau),$$

$$(A1)$$

where i and j are the coordinates inside the cluster impurity, and $\mathcal{G}^{-1}_{ij\sigma}$ is the Weiss field.

Within the cellular dynamical mean-field theory, the interacting lattice Green's function in the cluster-site basis is given by

$$G^{-1}_\sigma(i\omega_n) = \sum_k [i\omega_n + \mu - t(k) - \Sigma_\sigma(i\omega_n)]^{-1}, \quad \text{(A2)}$$

where $\omega_n = (2n + 1)\pi T$ are Matsubara frequencies, μ is the chemical potential, and $t(\mathbf{k})$ is the Fourier-transformed hopping matrix for the superlattice. Here, we consider two kinds of clusters, containing 6 sites and 12 sites, respectively [Fig. 1(a)]. For the six-site-clusters cas, the hopping matrix $t(k)$ of the cluster can be written as ($k \in$ the reduced Brillouin zone)

$$
\begin{bmatrix}
0 & t & t & 0 & t' * e^{-ik\cdot\delta(3)} & 0 \\
t & 0 & t & 0 & 0 & t' * e^{-ik\cdot\delta(4)} \\
t & t & 0 & t' & 0 & 0 \\
0 & 0 & t' & 0 & t & t \\
t' * e^{-ik\cdot\delta(1)} & 0 & 0 & t & 0 & t \\
0 & t' * e^{-ik\cdot\delta(2)} & 0 & t & t & 0
\end{bmatrix}, \quad \text{(A3)}
$$

where $\delta(1) = \vec{m} = (1 + \frac{\sqrt{3}}{2}, \frac{3}{2} + \sqrt{3})$, $\delta(2) = \vec{m} - \vec{n} = (-1 - \frac{\sqrt{3}}{2}, \frac{3}{2} + \sqrt{3})$, $\delta(3) = -\vec{m} = (-1 - \frac{\sqrt{3}}{2}, -\frac{3}{2} - \sqrt{3})$, and $\delta(4) = \vec{m} - \vec{n} = (1 + \frac{\sqrt{3}}{2}, -\frac{3}{2} - \sqrt{3})$ are the nearest-neighbor superlattice vectors.

Given the Green function for the effective medium $\mathcal{G}^{-1}_\sigma$, we compute the cluster Green function G_σ and the cluster self-energy Σ_σ, where $\mathcal{G}^{-1}_\sigma$, G_σ, and Σ_σ are described by $N_c \times N_c$ matrices. The effective medium $\mathcal{G}^{-1}_\sigma$ is then computed via the Dyson equation:

$$\mathcal{G}^{-1}_\sigma(\omega) = \left[\sum_k \frac{1}{\omega + \mu - t(k) - \Sigma_\sigma(\omega)} \right]^{-1} + \Sigma_\sigma(\omega). \quad \text{(A4)}$$

We iterate the dynamical mean-field theory self-consistent loop until the convergence of this procedure is achieved within, at most, 40 iterations.

In each iteration, in order to solve the effective cluster model and to calculate G_σ and Σ_σ, we use the weak-coupling interaction expansion continuous-time quantum Monte Carlo method [28]. At low T, the continuous-time quantum Monte Carlo method has a sign problem for this system even at half-filling, due to the absence of particle-hole symmetry. We typically use 1.92×10^7 quantum Monte Carlo sweeps to reach sufficient computational accuracy at low temperatures.

[1] T. Esslinger, Annu. Rev. Condens. Matter. Phys. **1**, 129 (2010).

[2] W. Hofstetter, J. I. Cirac, P. Zoller, E. Demler, and M. D. Lukin, Phys. Rev. Lett. **89**, 220407 (2002).

[3] I. Bloch, J. Dalibard, and W. Zwerger, Rev. Mod. Phys. **80**, 885 (2008).

[4] R. Jördens, L. Tarruell, D. Greif, T. Uehlinger, N. Strohmaier, H. Moritz, T. Esslinger, L. De Leo, C. Kollath, A. Georges, V. Scarola, L. Pollet, E. Burovski, E. Kozik, and M. Troyer, Phys. Rev. Lett. **104**, 180401 (2010).

[5] R. Jordens, N. Strohmaier, K. Gnther, H. Moritz, and T. Esslinger, Nature (London) **455**, 204 (2008).

[6] U. Schneider, L. Hackermller, S. Will, T. Best, I. Bloch, T. A. Costi, R. W. Helmes, D. Rasch, and A. Rosch, Science **322**, 1520 (2008).

[7] M. Imada, A. Fujimori, and Y. Tokura, Rev. Mod. Phys. **70**, 1039 (1998).

[8] P. W. Anderson, Science **235**, 1196 (1987).

[9] S. Kondo et al., Phys. Rev. Lett. **78**, 3729 (1997).

[10] M. Udagawa and Y. Motome, Phys. Rev. Lett. **104**, 106409 (2010).

[11] K. Takada et al., Nature (London) **422**, 53 (2003).

[12] S. Lefebvre, P. Wzietek, S. Brown, C. Bourbonnais, D. Jerome, C. Meziere, M. Fourmigue, and P. Batail, Phys. Rev. Lett. **85**, 5420 (2000).

[13] Y. Shimizu, K. Miyagawa, K. Kanoda, M. Maesato, and G. Saito, Phys. Rev. Lett. **91**, 107001 (2003).

[14] Z. Y. Meng, T. C. Lang, S. Wessel, F. F. Assaad, and A. Muramatsu, Nature (London) **464**, 847 (2010).

[15] L. Balents, Nature (London) **464**, 199 (2010).

[16] A. H. C. Neto, F. Guinea, N. M. R. Peres, K. S. Novoselov, and A. K. Geim, Rev. Mod. Phys. **81**, 109 (2006).

[17] H. Yao and S. A. Kivelson, Phys. Rev. Lett. **99**, 247203 (2007).

[18] A. Rüegg, J. Wen, and G. A. Fiete, Phys. Rev. B **81**, 205115 (2010).

[19] K. Sun, H. Yao, E. Fradkin, and S. A. Kivelson, Phys. Rev. Lett. **103**, 046811 (2009).

[20] Y. D. Chong, X. G. Wen, and M. Soljacic, Phys. Rev. B **77**, 235125 (2008).

[21] S. Uebelacker and C. Honerkamp, Phys. Rev. B **84**, 205122 (2011).

[22] Y. Z. Zheng et al., Angew. Chem. Int. Ed. **46**, 6076 (2007).

[23] J. Richter, J. Schulenburg, A. Honecker, and D. Schmalfuss, Phys. Rev. B **70**, 174454 (2004).

[24] J. Wen, A. Rüegg, C. C. J. Wang, and G.A. Fiete, Phys. Rev. B **82**, 075125 (2010).

[25] M. P. Shores, E. A. Nythko, B. M. Bartlett, and D. G. Nocera, J. Am. Chem. Soc. **127**, 13462 (2005).

[26] M. Sasaki, K. Hukushima, H. Yoshino, and H. Takayama, Phys. Rev. Lett. **99**, 137202 (2007).

[27] G. Kotliar, S. Y. Savrasov, G. Pálsson, and G. Biroli, Phys. Rev. Lett. **87**, 186401 (2001).

[28] A. N. Rubtsov, V. V. Savkin, and A. I. Lichtenstein, Phys. Rev. B **72**, 035122 (2005).

[29] E. Fradkin, S. A. Kivelson, M. J. Lawler, J. P. Eisenstein, and A. P. Mackenzie, Annu. Rev. Condens. Matter Phys. **1**, 153 (2010).

[30] M. Vojta, Adv. Phys. **58**, 699 (2009).

[31] M. Kohl, H. Moritz, T. Stoferle, K. Gunter, and T. Esslinger, Phys. Rev. Lett. **94**, 080403 (2005).

[32] E. Altman, E. Demler, and M. D. Lukin, Phys. Rev. A **70**, 013603 (2004).

[33] S. Folling, F. Gerbier, A. Widera, O. Mandel, T. Gericke, and I. Bloch, Nature (London) **434**, 481 (2005).

[34] T. L. Dao, A. Georges, J. Dalibard, C. Salomon, and I. Carusotto, Phys. Rev. Lett. **98**, 240402 (2007).

[35] I. Carusotto, J. Phys. B **39**, S211 (2006).

[36] Y. Furukawa, T. Ohashi, Y. Koyama, and N. Kawakami, Phys. Rev. B **82**, 161101 (2010).

[37] M. J. Lawler and E. Fradkin, Phys. Rev. B **75**, 033304 (2007).

[38] A. Georges, G. Kotliar, W. Krauth, and M. J. Rozenberg, Rev. Mod. Phys. **68**, 13 (1996).

[39] O. Parcollet, G. Biroli, and G. Kotliar, Phys. Rev. Lett. **92**, 226402 (2004).

[40] H. Yamase and W. Metzner, Phys. Rev. Lett. **108**, 186405 (2012).

[41] K. Sun and E. Fradkin, Phys. Rev. B **78**, 245122 (2008).

[42] H. Terletska, J. Vučičević, D. Tanasković, and V. Dobrosavljević, Phys. Rev. Lett. **107**, 026401 (2011).

[43] S. Okamoto, D. Senechal, M. Civelli, and A. M. S. Tremblay, Phys. Rev. B **82**, 180511(R) (2010).

[44] I. J. Pomeranchuk, Sov. Phys. JETP **8**, 361 (1959).

[45] C. J. Halboth and W. Metzner, Phys. Rev. Lett. **85**, 5162 (2000).

[46] M. Jarrell and J. E. Gubernatis, Phys. Rep. **269**, 133 (1996).

[47] E. V. Gorelik, I. Titvinidze, W. Hofstetter, M. Snoek, and N. Blumer, Phys. Rev. Lett. **105**, 065301 (2010).

[48] H. Park,, K. Haule, C. A. Marianetti, and G. Kotliar, Phys. Rev. B **77**, 035107 (2008).

[49] J. Zhao *et al.*, Nat. Phys. **5**, 555 (2009).

[50] S. Kasahara *et al.*, Nature (London) **486**, 382 (2012).

[51] V. Hinkov *et al.*, Science **319**, 597 (2008).

[52] R. Daou *et al.*, Nature (London) **463**, 519 (2010).

[53] A. Damascelli, Z. Hussain, and Z. X. Shen, Rev. Mod. Phys. **75**, 473 (2003).

[54] L. Limot, P. Mendels, G. Collin, C. Mondelli, B. Ouladdiaf, H. Mutka, N. Blanchard, and M. Mekata, Phys. Rev. B **65**, 144447 (2002).